

Switchable Ion Current Saturation Regimes Enabled via Heterostructured Nanofluidic Devices Based on Metal–Organic Frameworks

Gregorio Laucirica, Juan A. Allegretto, Michael F. Wagner, Maria Eugenia Toimil-Molares, Christina Trautmann, Matías Rafti,* Waldemar Marmisollé, and Omar Azzaroni*

The use of track-etched membranes allows further fine-tuning of transport regimes and thus enables their use in (bio)sensing and energy-harvesting applications, among others. Recently, metal–organic frameworks (MOFs) have been combined with such membranes to further increase their potential. Herein, the creation of a single track-etched nanochannel modified with the UiO-66 MOF is proposed. By the interfacial growth method, UiO-66-confined synthesis fills the nanochannel completely and smoothly, yet its constructional porosity renders a heterostructure along the axial coordinate of the channel. The MOF heterostructure confers notorious changes in the transport regime of the nanofluidic device. In particular, the tortuosity provided by the micro- and mesostructure of UiO-66 added to its charged state leads to iontronic outputs characterized by an asymmetric ion current saturation for transmembrane voltages exceeding 0.3 V. Remarkably, this behavior can be easily and reversibly modulated by changing the pH of the media and it can also be maintained for a wide range of KCl concentrations. In addition, it is found that the modified-nanochannel functionality cannot be explained by considering just the intrinsic microporosity of UiO-66, but rather the constructional porosity that arises during the MOF growth process plays a central and dominant role.

1. Introduction

In recent years, advances in nanotechnology and materials science have allowed the precise creation of different kinds of nanodevices with multiple applications. For instance, the construction of solid-state nanochannels (SSNs) that resemble

the properties exhibited by biological ion channels has attracted considerable attention in the scientific community representing a thrilling platform for basic and applied research.^[1] Similar to its biological counterpart, it is possible to develop SSNs with ion transport controlled by different stimuli.^[2–5] In addition, its iontronic output can be configured among different regimes such as ohmic, current saturation-controlled, or rectifying behavior which positions these systems as an interesting alternative for the creation of integrated ionic circuits.^[1]

One of the most established approaches to generating membranes with SSNs is the so-called ion-track etching technique. This procedure allows obtaining polymeric membranes with a high degree of control over the density (1 to 10¹¹ channels cm⁻²) and geometry of the nanochannels, which translates into a higher degree of control of ionic transport.^[6,7] Track-etched membranes have shown significant versatility

in many different fields, ranging from sensing to energy harvesting.^[8–12] Notably, it is possible to fine-tune the iontronic response of the device by modifying the shape of the nanochannel by properly setting the etching conditions, changing the physicochemical properties of the channel surface by chemical modification, or by the combination of both in a rational manner. These approaches were successfully employed for the creation of nanodevices with ion transport controlled by different stimuli such as pH, external voltage, light, temperature, etc.^[13–15] In most of these examples, the underlying mechanism relies on tuning the transport properties by charge and/or size exclusion phenomena. Precisely, when searching for materials for their integration into nanodevices (which should allow both charge and size exclusion), Metal–organic frameworks (MOFs) come to mind as prospective candidates to reduce the pore dimensions and add new physicochemical properties to the nanochannel.^[16,17]

MOFs are coordination networks constituted by metal ions and organic linkers featuring tremendous versatility regarding their physicochemical properties.^[18,19] Among them, synthesis and characterization of those with permanent porosity are being extensively explored and applications in different fields

G. Laucirica, J. A. Allegretto, M. Rafti, W. Marmisollé, O. Azzaroni
Instituto de Investigaciones Físicoquímicas Teóricas y Aplicadas (INIFTA)
Departamento de Química
Facultad de Ciencias Exactas
Universidad Nacional de La Plata
CONICET, CC 16 Suc. 4, La Plata B1904DPI, Argentina
E-mail: mrafti@quimica.unlp.edu.ar; azzaroni@inifta.unlp.edu.ar

M. F. Wagner, M. E. Toimil-Molares, C. Trautmann
GSI Helmholtzzentrum für Schwerionenforschung
64291 Darmstadt, Germany
C. Trautmann
Technische Universität Darmstadt
Materialwissenschaft, 64287 Darmstadt, Germany

 The ORCID identification number(s) for the author(s) of this article can be found under <https://doi.org/10.1002/adma.202207339>.

DOI: 10.1002/adma.202207339

are reported,^[20] including energy conversion and storage,^[21,22] biosensing,^[23–25] nanofiltration,^[26,27] just to name a few relevant examples. The advantages of integration between MOFs and SSN have not gone unnoticed; by pushing down the channel dimensions and introducing well-defined porosity and tailored chemical moieties in the SSN membrane, these nanodevices were successfully employed for selective transport of ions, including alkaline metals^[28–30] and fluoride;^[31] unidirectional transport of protons;^[32–35] gas separation applications,^[36] and even osmotic energy generators.^[37] However, to the best of our knowledge, the exploitation of MOF/SSN architectures for the development of stimuli-responsive nanodevices has been not yet fully described. Considering this, the possibility of alternation between different transport regimes triggered by an external stimulus is still a highly relevant and challenging goal. On the other hand, textural properties other than intrinsic microporosity of the MOF phase are typically not considered when trying to account for the origin of the transport regime thus overlooking its significant contribution. It has been already reported that MOF phases showcase two general porous domains that contribute to (and control) transport regimes: an intrinsic microporosity, determined by MOF crystalline structure, and the so-called constructional porosity, arising from defects and the coalescence of growth fronts during synthesis.^[38] It has been shown, for example, that constructional porosity can endow wider and more hydrophilic porosity to intrinsically hydrophobic ZIF-8 films, allowing for differential adsorption of water and methanol,^[39] and allowing the permeation of redox probes otherwise unable to access the MOF microporosity.^[40]

Herein, we present the fabrication of a MOF-modified membrane by confined synthesis of zirconium and terephthalic acid-based UiO-66 MOF inside of a poly(ethylene terephthalate) (PET)-based single bullet-shaped nanochannel. The MOF confined synthesis was carried out by asymmetric interfacial growth method; i.e., MOF precursors were separated by a track-etched membrane, exposing the nanochannel tip (the smallest opening) to the terephthalic acid (benzene-1,4-dicarboxylic acid, BDC) solution and the base (the wider opening) to the Zr⁴⁺ solution. Under these conditions, we have found that the resulting UiO-66 MOF fills the nanochannel, but is different from the most simplistic scenario in which a homogeneous quasi-monocrystalline strictly microporous phase is assumed, and a superimposed heterostructure dependent on the axial coordinate arises. Such heterostructure due to MOF precursors mixing effects yields an additional mesoporosity, known as constructional porosity (CP), which must be considered in order to understand the transport regimes established upon application of transmembrane potentials. In addition, we have found that ion transport through the hereby presented MOF-modified nanochannels is dominated by both charge exclusion and hierarchical porosity of UiO-66 (a combination of both, micro- and constructional porosity). Our results indicate that by generating a 3D network of pathways for the ions to diffuse through, an ion depletion zone would appear. Consequently, this MOF-filled nanochannel showcases an iontronic output characterized by ion current saturation for transmembrane voltages higher than $\approx \pm 0.3$ V. This new iontronic behavior differs from the typical ohmic or diode-like behaviors found in bullet-shaped nanochannels and can be reversibly switched on/off by adjusting

either the pH or the ionic strength which positions this platform as an interesting alternative for the design of ionic circuits and logical devices.

2. Results and Discussion

Confined synthesis of UiO-66 MOF was performed in ion-track etched bullet-shaped nanochannels membranes by asymmetric interfacial growth. To this end, the PET membrane was mounted in between a two-body Teflon cell, and each cell body was filled with one of the MOF precursor solutions (i.e., Zr⁴⁺ on the base side and BDC on the tip side of the membrane) as schematized in **Figure 1a**. By doing so, exposed carboxylate moieties from the PET membrane serve as anchoring points that will trigger UiO-66 heterogeneous confined nucleation and subsequent growth.^[41–43] The system was then placed in an oven at 80 °C for 14 h.^[44] After synthesis, the membrane used for MOF synthesis (hereinafter PET/UiO-66) was washed three times with dimethylformamide (DMF), ethanol, and Milli-Q water, respectively.

As schematized in **Figure 1b**, UiO-66 is composed of BDC linkers connected to oxyhydroxide Zr clusters. A pristine UiO-66 phase will have each hexanuclear Zr cluster connected to 12 BDC linkers, leading to an fcu net, with a chemical formula of $[\text{Zr}_6\text{O}_4(\text{OH})_4][\text{C}_6\text{H}_4(\text{COO})_2]_6$. This arrangement generates octahedral cages of 1.1 nm diameter, and tetrahedral cages of 0.8 nm diameter, in a 1:2 ratio. These micropores are connected by 0.6 nm triangular windows.^[45–47] Achieving a crystalline UiO-66 phase is of paramount importance since it determines the intrinsic microporosity, as schematized in **Figure 1b**. X-ray diffraction (XRD) experiments on PET/UiO-66 membrane revealed the presence of MOF phase with the expected fcu topology, with clear diffraction peaks ascribable to the (111), (200), and (220) planes at $2\theta = 7.44^\circ$, 8.60° , and 12.08° respectively, in good agreement with bulk-synthesized powder and predicted diffraction pattern (**Figure 1c**). For most synthetic conditions, it is unlikely to obtain a completely perfect structure, as random linkers^[46] and metallic clusters^[48] might be missing, generating defects across the structure. Defects can become regular, happening in an ordered fashion (from correlated nanoregions to a global scale) that may be evidenced by anomalous diffraction peaks at the XRD pattern.^[48,50] Moreover, some defects can also lead to pore diameters higher than 1.1 nm.^[49] In the present case, the obtained diffraction patterns indicate that synthetic conditions yield a material that retains the fcu topology of pristine UiO-66. Furthermore, N₂ adsorption isotherms are consistent with the typical UiO-66 intrinsic microporous domains, with no additional porosity above 1.1 nm diameter (see Supporting Information file). Additional discussion on the presence of defects in the UiO-66 structure is presented in the Supporting Information file together with an estimation of the number of linker defects by thermogravimetric analysis.

To study the ion-transport properties of the nanofluidic device, the membrane is mounted in between a two-body Teflon cell filled with an electrolyte solution. Then, a four-electrode arrangement is connected to a potentiostat to apply a sweep transmembrane voltage (V_t) program and, simultaneously,

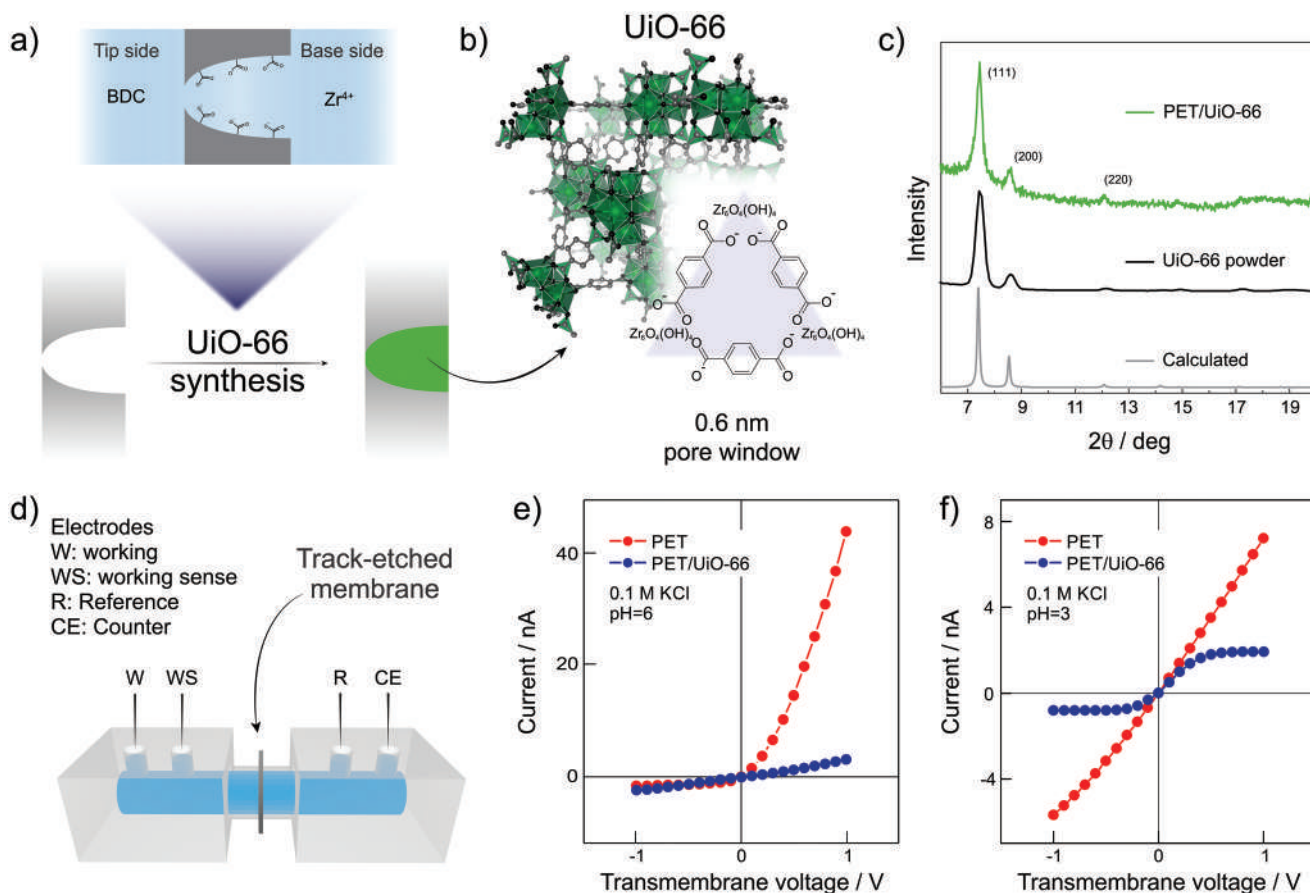


Figure 1. a) Schematic illustration of confined interfacial synthesis of b) UiO-66 MOF. c) X-ray diffraction patterns for the calculated (gray), bulk-synthesized UiO-66 powder (black), and PET/UiO-66 membrane (green). d) Electrochemical cell and electrode arrangement employed for the iontronic measurements. e, f) $I-V$ curves for bare and PET/UiO-66 membranes in 0.1 M KCl measured at pH 6 (e) and pH 3 (f).

record the ion current (Figure 1d). By analyzing the relationship between the transmembrane voltage and the ionic current it is possible to infer the characteristics of the ionic transport through the nanochannels. The current–voltage curve ($I-V$ curve) of a bare bullet-shaped single nanochannel in 0.1 M KCl (pH \approx 6) solution is characterized by a rectifying behavior with the high conductance branch at the positive transmembrane voltage (working electrode on the tip side, Figure 1e). As previously reported, this behavior can be explained by considering the interplay between the asymmetric geometry and nanometric opening together with the presence of negatively charged carboxylate moieties on the PET surface.^[51] In terms of functionality, the integration of UiO-66 leads to an appreciable decrease in the current as shown in Figure 1e. In addition, the inclusion of MOF within nanopore space promoted a drop in the rectification efficiency ($I(1\text{ V})/I(-1\text{ V})$) from 26.8 to 1.7, which indicates that the material modifies the operating ionic-transport regime. However, the response of both the PET and the PET/UiO-66 membranes is completely different in terms of transport regime for acidic pH conditions. When employing a 0.1 M KCl solution at pH 3, the $I-V$ curve for the bare PET membrane displays an almost ohmic behavior which can be attributed to the absence of surface charge due to the protonation of carboxylate moieties from PET (see Figure 1f). On the

other hand, the iontronic output of the PET/UiO-66 membrane at pH 3 features an ion current saturation (ICS) region for $|V_t| > 0.3$ V where the current is almost maintained invariant when V_t is further increased. The presence of such a saturation regime is unusual in bullet-shaped nanochannels and has been explained in other nanofluidic systems by resorting to concentration polarization effects. This ICS regime has been typically observed in two kinds of nanochannels: channels with the same surface charge polarity at both ends but the opposite charge in the middle zone (e.g., bipolar transistors), or channels with a cigar or biconical geometries.^[52–54] However, similar behavior has been also reported in other microfluidic membranes modified with hierarchically structured materials as a result of the interplay between the ion selectivity and the severe confinement provided by the porous environment.^[55–57] For these cases, the interpretation given for the saturation current curves obtained relied on the concentration polarization phenomenon. The narrow and charged pores arising from the modification, generate counterion enrichment and co-ion exclusion. Upon the application of a given transmembrane voltage, cations are expected to be transported to the negative electrode whereas the anions experience the opposite effect. However, if the membrane presents ion selectivity, the transport of co-ions is drastically restricted due to the permselectivity of the

narrow-charged mesoporous environments within the membrane. As a consequence of such phenomenon, the ion concentration is augmented at the surface of one face of the membrane and depleted on the other face, producing a concentration gradient that causes the transport to become independent of the applied transmembrane voltage. A detailed discussion of this transport mechanism can be found elsewhere.^[56,58–61] Let us consider the case of an anion permselective membrane as an illustration. In that case, the anodic side features an increment in the ionic concentration whereas the cathodic side shows a depletion of the ionic concentration. If the gradient due to the concentration polarization is pronounced, the transport in the boundary layers becomes diffusion-controlled and the I - V curve is characterized by the presence of a limiting current (i.e., saturation current) above a certain voltage threshold. The sigmoidal I - V curves observed for such heterostructured membranes resemble the I - V curves found here for the PET-UiO-66 membranes at low pH conditions. Therefore, the ion current saturation behavior observed for the MOF-filled nanochannels could be ascribed to the concentration polarization caused by a combination of two effects: a narrow porosity in addition to the surface charge of the UiO-66 at acidic conditions causing a marked permselectivity. To gain further insight into the ion selectivity of PET/UiO-66 membranes, I - V curves were recorded under asymmetric KCl conditions at pH 3.^[62,63] Results available in the Supporting Information file show that the contribution of chloride anions to the current widely exceeds the potassium current which is indicative of an anion-selective behavior, in line with previous reports.^[31,64]

Regarding the role of the UiO-66 porosity on the ion transport, it is worth noticing that, except for perfect crystalline MOF phases, additional pathways can exist for the ionic transport apart from those coming from the intrinsic microporosity (typically below 2 nm diameter). Such additional pathways are typically generated during the growth process as a combination of defects and the coalescence of growth fronts emerging from nucleation points, yielding voids within the mesoporosity size range (above 2 nm), also known as constructional porosity.^[38,39] Since related to nucleation and growth processes, it is expected that constructional porosity is affected by experimental conditions used during synthesis, such as the metal/linker ratio. In this regard, the confined synthesis method employed in this work involves differences in metal and linker concentrations across the nanochannel thus generating different synthesis conditions along the nanochannel axis. In particular, the higher concentration of the BDC linker acts as stabilizing agent on the tip side, thus creating smaller entities, while its lower concentration on the base side (concomitantly with a higher concentration of Zr^{4+}) allows for a more extended growth of the MOF units,^[65] as confirmed by scanning electron microscopy (SEM) images of tip and base side of the membranes (see **Figure 2** and Supporting Information). This is in line with general trends reported for MOFs^[66] and particularly with a relatively recent article where UiO-66 nucleation and growth mechanisms were explored by pair distribution function analysis.^[67] These authors have suggested that upon dissolution, Zr^{4+} forms the hexanuclear cluster that will be later assembled by coordination with BDC linkers, to finally form the MOF phase. Thus, the relative excess of one or another at each side of the membrane affects

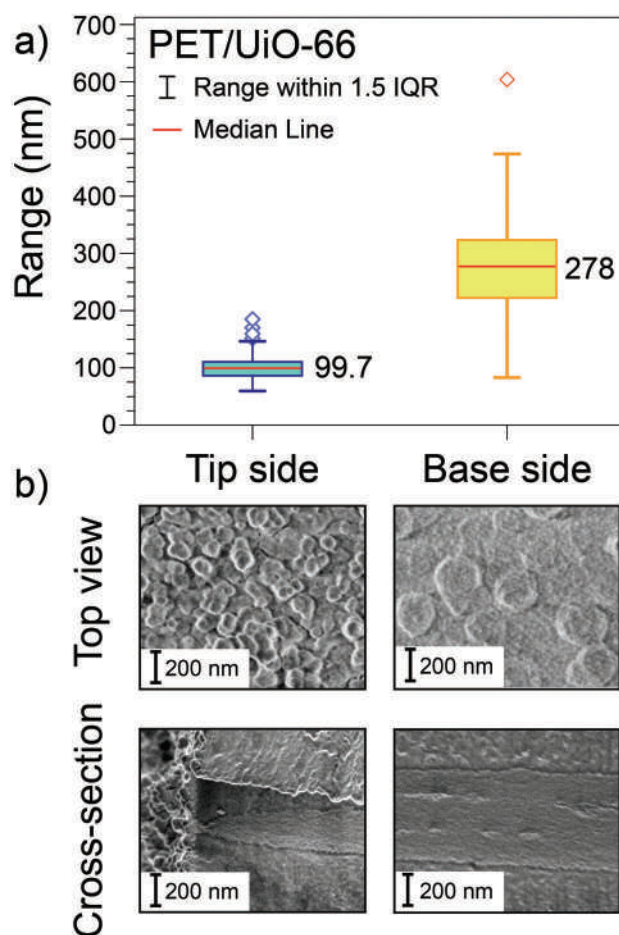


Figure 2. a) Distribution of Feret's diameter for particles at both sides of the PET/UiO-66 membranes (tip and base side). b) Top and cross-section SEM images of tip and base side of the PET/UiO-66 membrane. Full images can be found in the Supporting Information.

the nucleation and growth process. Being both metal and linker concentrations are variable along the nanochannels during the synthesis, differences in the constructional porosity along the channel axis are also expected. Notoriously, and despite such existing asymmetry, cross-section images with secondary and backscattered electrons, revealed a nanochannel filled with the MOF phase. Even further, energy-dispersive X-ray (EDX) analysis reveals a continuous distribution of Zr across the nanochannel. It is possible now to analyze the effect of the heterostructure and selectivity phenomena on the iontronic output in more detail.

Typically, the symmetry of the iontronic output is related to the symmetry of the nanochannel. In particular, symmetrical systems such as cylindrical channels feature a symmetric I - V curve (e.g., an ohmic behavior in the case of cylindrical channels) whereas asymmetric charged channels usually show an asymmetric I - V curve characterized by a difference in the currents obtained at the same magnitude of the transmembrane voltage but opposite polarity (i.e., rectifying behavior, as in the case of bullet-shaped nanochannels).^[1,68] In this scenario, an analysis of the iontronic output symmetry can help to infer conclusions

about the symmetry of the channel and the MOF heterostructure. To this end, UiO-66 was also synthesized by inverting the configuration used for positioning of precursors; i.e., Zr^{4+} solution was placed in the tip side compartment whereas the BDC solution was placed in the base side compartment (experiments performed on this membrane will be hereinafter referred to as PET/UiO-66-Inverted). By comparatively analyzing the normalized $I-V$ curves for both synthesis configurations (Figure 3a,b), it can be seen that the ratio between saturation currents at positive and negative transmembrane voltages depends on the synthesis configuration. Specifically, when the BDC solution is placed in the tip side compartment, the $I-V$ curve displays the highest saturation current (I_{max}) at positive transmembrane voltages (Figure 3a). However, when the BDC solution is placed in the base side compartment, the highest saturation current is obtained at negative transmembrane voltages (Figure 3b). Now, as previously mentioned, the iontronic response does not only depend on the charge but also on the shape of the nanochannel; in particular, pristine bullet-shaped nanochannels present asymmetric $I-V$ curves.^[51] For this reason, to discard the effect of the bullet geometry on the asymmetry of the response obtained for the MOF-filled nanochannels, PET/UiO-66 membranes were also prepared in PET membranes with cylindrical nanochannels (hereinafter PET/UiO-66-Cylindrical), which initially behave like ohmic resistors; i.e., exhibit symmetric and linear $I-V$ curves (see Supporting Information).

Despite the geometric symmetry of the channel, PET/UiO-66-Cylindrical also evidences an ICS behavior with asymmetric currents as can be seen in Figure 3c. Further analysis can be performed by comparing the normalized curves ($I/|I_{max}|$ versus V_t) shown in Figure 3. The asymmetry in the saturation currents is rather similar for all conditions employed; i.e., bullet-shaped-based PET/UiO-66 membranes reach a pla-

teau for $I/|I_{max}| = |0.78|$, while PET/UiO-66-Cylindrical reach it at $I/|I_{max}| = |0.71|$. Altogether, these facts provide evidence for different characteristics featured by the system: i) the geometry is not the most determinant factor for the transport regime of MOF-filled nanochannels (although, it is worth mentioning that the ICS behavior was more pronounced in the asymmetric channels which could be ascribed to the narrower tip opening); ii) Ionic transport in the MOF-filled nanochannels is mainly governed by chemical and structural features endowed by the MOF phase; iii) Intrinsic MOF microporosity, if involved, is not the only factor determining the ionic transport through the modified nanochannel. The last statement can be rationalized as follows; microporosity is strictly dependent on the crystalline structure of considered MOF and should not depend on synthetic conditions provided any changes in topology are generated, as discussed above (which was checked by means of XRD, see Supporting Information file for further discussion of this topic). On the other hand, the highest saturation current values are obtained when the positive electrode is placed in the compartment corresponding to the membrane face exposed to the Zr^{4+} solution during the MOF synthesis, independently of the nanochannel geometric asymmetry. This fact reinforces the idea that ionic transport is also determined by the constructional porosity (mesoporosity) as it is the only porosity that is expected to be different along the nanochannel.

2.1. Influence of the pH on the Iontronic Output

Typically, it is assumed that the changes in the ion transport through nanochannels can be transduced into readable ion signals if the stimulus trigger variations in the surface charge, wettability, or inner volume of the channel.^[1,9] In particular, for

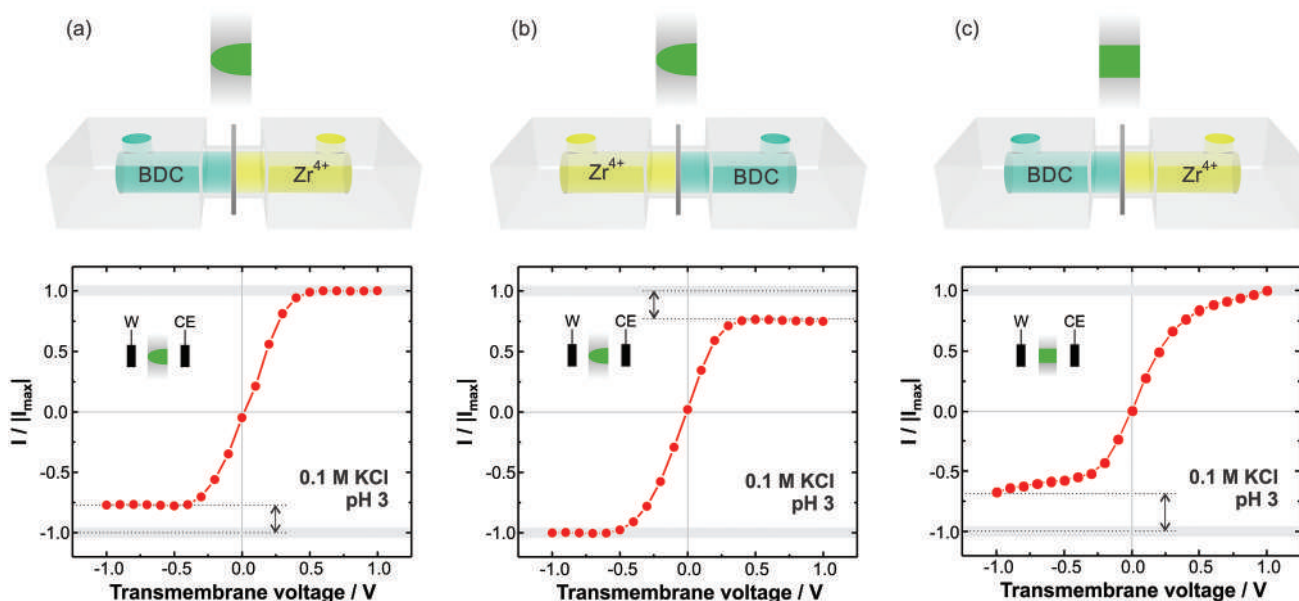


Figure 3. Scheme of the two different synthesis configurations for bullet-shaped nanochannels with their resultant iontronic output. a) BDC and Zr^{4+} are placed on the tip and base side respectively. b) BDC and Zr^{4+} are placed on the base and tip sides respectively. c) Scheme of synthesis configuration with cylindrical nanochannel (200 nm diameter) and the corresponding iontronic output. In all the presented scenarios, the position of the working electrode (W) during the iontronic output measurement is pictured in the top left corner (reference electrodes at both sides were avoided for simplicity).

the case of nanofluidic devices with surface groups that contain acid–base equilibria associated, a simple way to modulate the iontronic output and study the transport basis is by changing the pH conditions.^[69,70] Therefore, to gain insight into the origins of the ion transport regime, the iontronic output for the PET/UiO-66 membrane (bullet-shaped single nanochannel, prepared as indicated in Figure 1) was studied at different pH values. As it can be seen in Figure 4a, modifying the pH of the media causes changes in the operating transport regime. Although there is an enhanced conductance at positive transmembrane voltages, the shape of the I – V curve differs from the typical rectifying behavior exhibited by the pristine PET membrane, particularly in the acidic pH range. Thus, for 0.1 M KCl solutions with $\text{pH} < 4.5$, the I – V curves display an ICS region for $|V_t| > 0.2$ V where the current is almost maintained invariant as $|V_t|$ is further increased. As previously mentioned, an ICS regime can result from the combination of multiple narrow pathways arising from the porous nanostructure of the MOF and the ion permselectivity caused by a high surface charge of the porous walls (see below) leading to a depletion zone inside the channel. Thus, for $\text{pH} < 4.5$, the iontronic output not only keeps the ICS behavior but also, the conductance does not present appreciable changes in terms of pH (Figure 4b). When the

pH value is between 4.5 and 7.5, the I – V curve is characterized by an almost linear behavior that could be attributed to the loss of the charge. This reinforces the previous hypothesis in which saturation is explained by an interplay between porosity and ion selectivity. Consequently, the rupture of the depletion-governed behavior leads to an increase in conductance as the pH is increased. Finally, for alkaline conditions ($\text{pH} > 8$), the iontronic response exhibits a slight curvature at high transmembrane voltages which could be ascribed to the appearance of a new selective regime but now, due to the presence of negatively charged sites. Concomitantly, an attenuation in the conductance values is generated.

In opposition to the diode-like rectifying transport behavior, in the case of the ICS regime, it is not possible to directly correlate the shape of the I – V curve with the sign of the nanochannel surface charge. These estimations are even more intricate when considering the proposed asymmetry of the MOF structure along the axial coordinate. To address this issue, measurements of reversal potential (V_{rev}) at different pH values were performed to estimate the transference number (i.e., the fraction of current transported by cations or anions) and thus, to draw conclusions about the trend presented in Figure 4b.^[8,71] For these experiments, the membrane was placed in the electrochemical cell and then,

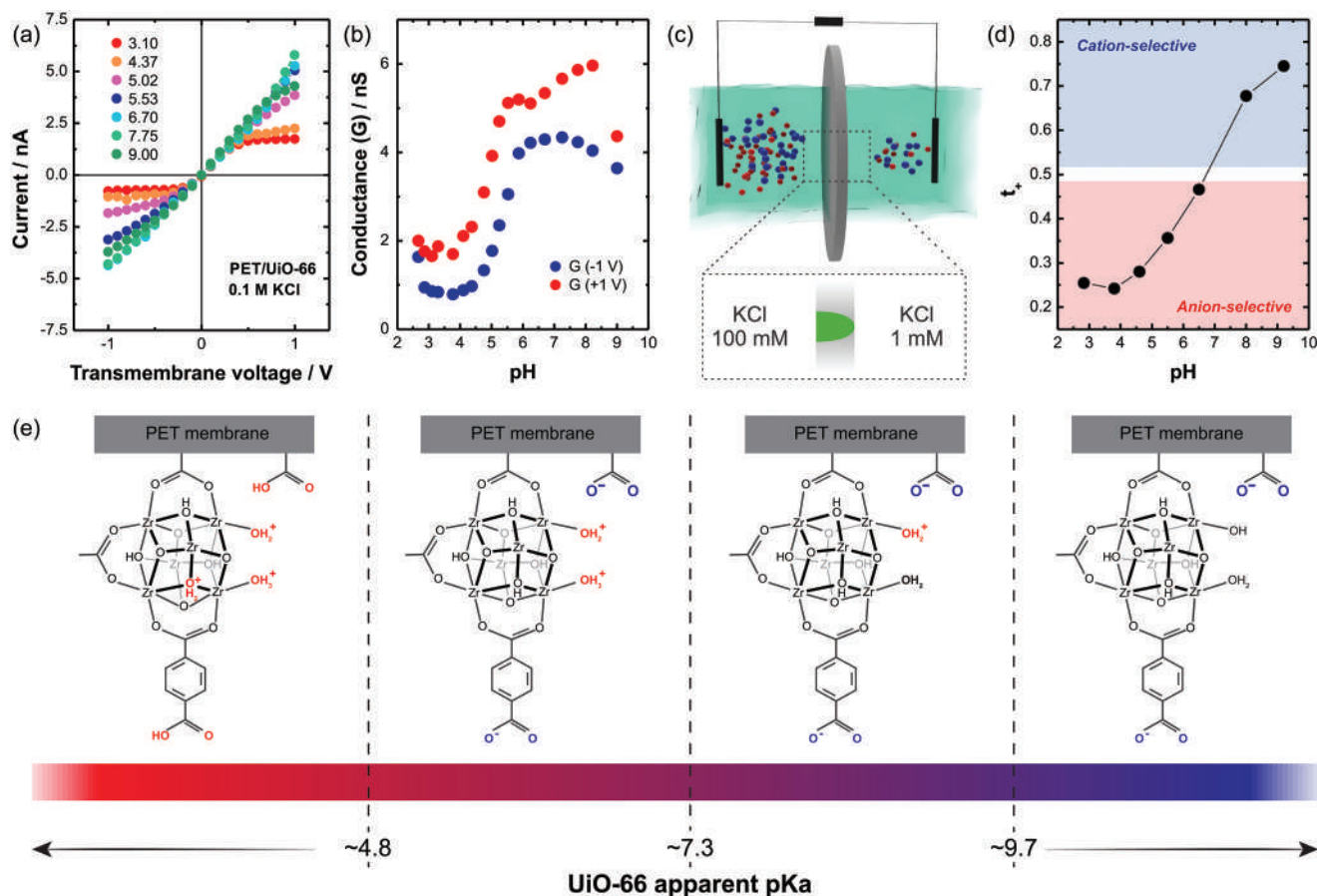


Figure 4. a) I – V curves for the UiO-66-modified membrane at different pH conditions. b) Conductance (G) values at ± 1 V as a function of pH. c) Scheme of the experimental set-up for the cation transference measurements. In all the cases, 10^{-3} M and 0.1 M KCl solutions were placed in the tip and base reservoir, respectively. d) Cation transference number for different pH conditions e) Scheme illustrating the different acid–base equilibria involved in the PET/UiO-66 membrane. Numbers correspond to apparent pKa values obtained by acid–base potentiometric titration for these equilibria.

exposed to a 100-fold concentration gradient (Figure 4c) (for further details about experimental set-up and transference number estimation, see Supporting Information file). Under this configuration, the open-circuit voltage (i.e., V_{rev}) was recorded at different pH values by employing a four-electrode set-up, and then, with this parameter in hand, the transference numbers were estimated (t_+ : cation transference number; t_- : anion transference number. As always, $t_+ + t_- = 1$). Typically, $t_+ < 0.5$ (or $t_- > 0.5$) indicates an anion-selective regime whereas an $t_+ > 0.5$ (or $t_- < 0.5$) implies a cation-selective behavior. Finally, the ion transport is not selective when both t_+ and t_- take values of ≈ 0.5 .^[71] As can be seen in Figure 4d, the value $t_+ = 0.25$ ($t_- = 0.75$; $V_{\text{rev}} \approx -58$ mV) evidences a transport governed by a positively charged surface at pH = 3. The increment of the pH value to 6.5 generates an attenuation in the reversal potential around -8 mV which is indicative of an almost non-selective behavior as indicates the value $t_+ = 0.47$. Finally, when the reversal potential is evaluated at pH above 6.5, V_{rev} displays not only a sign inversion but also an appreciable increment in magnitude, reaching a 58 mV value for pH = 9.1, thus indicating anion-selective behavior as suggested by $t_+ = 0.75$ value. As discussed for data presented in Figure 4b, the plot exhibits a region for pH values between 2 and 4 where the conductance is maintained almost invariant as the pH increases due to a behavior controlled by the ICS regime. This observation is in line with the results obtained for t_+ , where the cation selectivity is also maintained without appreciable changes at very acid pH values. In the region $5 < \text{pH} < 7.5$, the depletion-governed transport is lost, i.e., the saturation regions are disrupted, which promotes a conductance increment with increasing pH values. Also, in this region, the transference number analysis evidences a loss of selectivity which explains the depletion zone disappearing due to the attenuation in the concentration polarization phenomenon. Finally, for $7.5 < \text{pH} < 9$, the conductance values present a slight diminution for increasing pH. Considering the analysis in terms of t_+ , such effect could be ascribed to an increment in the ion selectivity and consequently, the appearance of a low concentration polarization but, in this case, due to the prevalence of negatively charged sites ($t_+ > 0.5$).

To support the conclusions on the interplay between selectivity and the porosity in the MOF-filled channels inferred from the I - V behavior at different pH values, the acid-base chemical nature of the MOF needs to be considered. Figure 4e schematizes the different acid-base equilibria reported for the UiO-66. Results

obtained for pH values lower than ≈ 6.5 show that the current is mainly transported by anions (anion-selective transport), indicating a positive pore surface charge. This is in line with previous reports indicating a prevalence of positively charged sites in the UiO-66 due to the multiple acid-base equilibria of Zr-OH_2^+ .^[64,72] Thus, such positive surface charge of the mesoporous environments arising from MOF filling provides the anion selectivity which gives rise to the saturation current-controlled behavior. If the pH condition is ≈ 6.5 , the membrane behaves as non-selective, as indicated by the cation transference number ≈ 0.5 . The selectivity loss triggers the rupture of the saturation current-controlled regime since, in absence of net charge, the concentration polarization phenomenon does not occur. Finally, at basic pH values, the membrane features cation-selectivity ($t_+ > 0.5$) due to the prevalence of negatively charged sites, as suggested by pKa values obtained from UiO-66 acid-base potentiometric titration experiments (see Supporting Information file). The increment in selectivity (cation selective transport) generates again an attenuation of the current for high transmembrane voltage values due to the concentration polarization phenomenon. The strong correlation between the changes in the iontronic output with pH and the acid-base equilibria of the UiO-66 surface groups supports the idea of an interplay between both the MOF heterostructure and its surface charge distribution along the nanochannel as responsible for the peculiar transport behavior observed in the synthesized membranes.

2.2. Influence of Electrolyte Concentration

The combination of nanoscale confinement and charged surfaces promotes profound changes in ion transport regarding the expected behavior for macroscopic length scales. Some of these particular effects can be studied when the iontronic output of SSNs is evaluated at different bulk electrolyte concentrations. Figure 5 shows the I - V curves at different KCl concentrations for two different conditions, pH 3 and 6. At pH 3, the I - V curves show the above-discussed ICS behavior in the range from 1 to 3000×10^{-3} M for KCl concentration (Figure 5a). Higher transmembrane voltages are needed to reach the saturation current as the ion concentration in the solution increases. Particularly for 3000×10^{-3} M KCl, although it is possible to see a clear attenuation at high

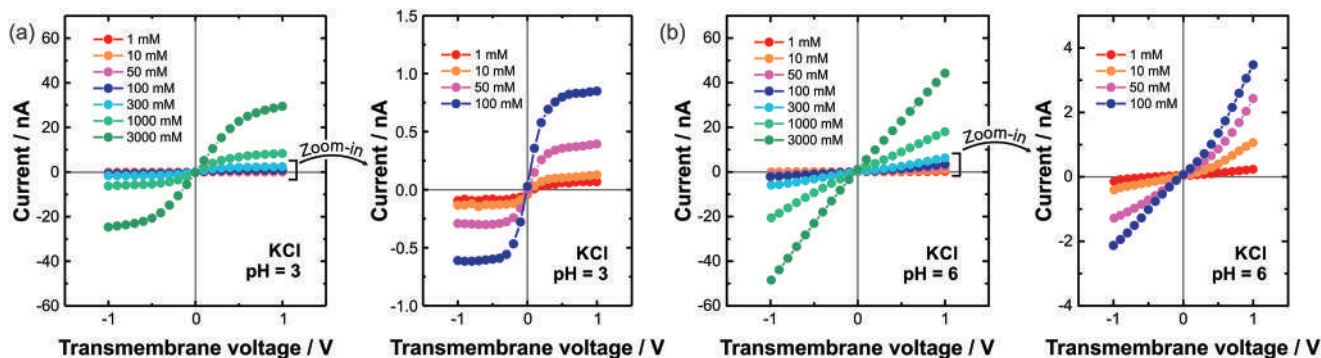


Figure 5. a) I - V curves for the UiO-66-modified membrane at different KCl concentrations at pH 3. Zoom-in shows the I - V for low KCl concentrations. b) I - V curves for the UiO-66-modified membrane at different KCl concentrations at pH 6. Zoom-in shows the I - V for low KCl concentrations.

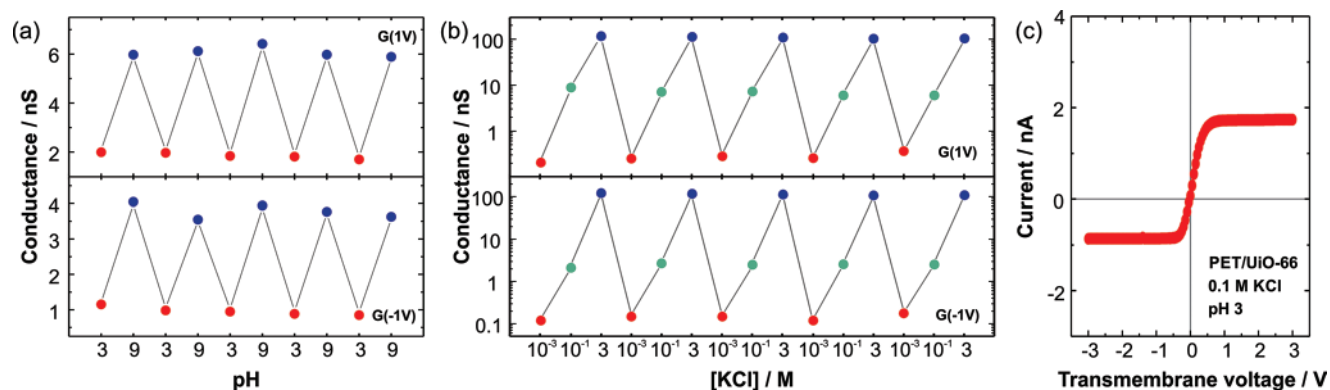


Figure 6. a) Conductance values at ± 1 V obtained in the pH reversibility test. In both cases, the measurements were performed in 0.1 M KCl. b) Conductance values at ± 1 V were obtained in the electrolyte concentration reversibility test. In all cases, the measurements were performed at pH 6. c) I - V curve at pH 3 in an extended voltage window.

transmembrane voltage, the current does not reach a saturation constant value. This is consistent with the occurrence of ion depletion zone inside the pores caused by the transmembrane voltage. In this regard, higher transmembrane voltages are needed to produce the depletion at higher salt concentrations. As previously mentioned, the ICS behavior cannot be explained only by the narrow pathways inside the channel but electrostatic exclusion imposed by the charged UiO-66 surface needs to be also considered. Thus, the large increment of KCl concentration in the 3000×10^{-3} M solution produces an efficient screening of the surface charge that leads to an attenuation of ion-selective properties and concomitantly, to a partial loss of the ICS behavior.^[55]

For $\text{pH} \approx 6$, the PET/UiO-66 membrane presents an iontronic behavior with a slight deviation from what is expected in ohmic resistors at KCl concentrations ranging from 1 – 300×10^{-3} M (Figure 5b). This is in agreement with the low charge state of the MOF surface that hinders the appearance of the ICS regime, in line with the previous discussion. Then, if salt concentration is increased to values ≈ 1000 – 3000×10^{-3} M, the I - V curve exhibits the typical ohmic behavior expected in the bulk regime, ascribable to an efficient surface charge screening.^[73] This final result supports the hypothesis that the multiple pathways arising from the constructional porosity alone are not the only factor affecting the transport regime, and that there is a strong interplay between both, the heterostructure and the charge distribution of UiO-66 along the nanochannel.

2.3. Stability and Reversibility

In view of possible further developments of MOF-modified SSNs, which include technological applications in different fields such as electronic,^[74] ion sieving,^[29,31] energy conversion,^[37] and biosensing,^[12] reversibility of the observed pH- and electrolyte concentration-dependent behavior is highly desirable. This is particularly challenging for architectures including MOFs since extreme pH values and high ionic strength conditions were shown in the past to induce damage (either partial dissolution of the material, porous framework collapse, changes in surface charge, or a combination of all the mentioned

effects).^[75–78] For this reason, changes in the initial response of the PET/UiO-66 membrane were analyzed in terms of conductance, by exposing the membrane to 0.1 M KCl solutions at pH 3 and pH 9, alternately for five cycles (Figure 6a). The analysis in terms of conductance values at ± 1 V shows good reversibility which would allow not only to discard alterations caused by disruption of MOF structure within the channel but also irreversible changes in the UiO-66 structure due to the extreme pH values. This was also verified by XRD analysis, revealing that crystallinity is preserved after exposure of UiO-66 powder to such conditions (see Supporting Information).

Analogously, the same modified membrane was alternately exposed to 1, 100, and 3000×10^{-3} M KCl concentrations at fixed pH (≈ 6) for five cycles (Figure 6b). The analysis in terms of the conductance shows that the iontronic output is not affected by exposure to high ionic strength, suggesting that chemical and structural properties of UiO-66 MOF are maintained for the whole range of KCl concentrations used. More interestingly, it is possible to discard MOF leaching even at 3000 mM KCl which could be ascribed to the highly-stable attachment of the particle to the channel walls due to the coordination of Zr centers with PET-exposed carboxylate moieties.

Additionally, it has been shown that ICS regimes can be disrupted if a sufficiently high transmembrane voltage is applied.^[57–59] For this reason, ion transport across the nanofluidic device was also studied in a wider transmembrane voltage window. Remarkably, PET/UiO-66 membrane retains its ICS regime even in the range between ± 3 V, as can be seen in Figure 6c. The stability of the ICS regime toward an extended transmembrane voltage window becomes of critical importance when aiming to integrate a nanofluidic device into different platforms.

3. Conclusions

The creation of a UiO-66-modified single PET nanochannel with exceptional stability and ion transport control has been described. By employing the asymmetric interfacial growth method, the track-etched nanochannel is filled with MOF UiO-66. The MOF-filled nanochannels displayed an ion transport

regime characterized by a saturation current region for transmembrane voltages higher than 0.3 V in acidic conditions. This unusual behavior for bullet-shaped nanochannels can be interpreted as a consequence of the interplay between the permselectivity produced by the surface charge and the presence of narrow pathways provided by the MOF heterostructure.

Moreover, I - V curves are not symmetric, and the value of the saturation currents depends on the membrane orientation during the MOF synthesis. Due to the asymmetric synthesis conditions, a heterogeneous structure of the MOF along the axial axis is expected. Notably, this structure asymmetry, arising from the different local concentrations of metal and linker at both sides of the membrane during synthesis, determines the symmetry of the I - V curve independently of the orientation of the bullet-shaped nanochannel. These results strongly suggest that microporosity alone is not enough to explain the iontronic output of the system, which would be also dictated by the constructional porosity.

Furthermore, the ionic current saturation behavior can be reversibly switched ON/OFF by changing the solution pH and the ICS-controlled iontronic output could be maintained even in 3000×10^{-3} M KCl solutions. In addition, the UiO-66-modified membrane preserves its ionic response after the exposition to different pH (between 3 and 9) and KCl concentrations (between 1 and 3000×10^{-3} M) which demonstrate acceptable stability of the MOF inside of the channel to different operative conditions. We believe that this kind of device can be an interesting alternative for the design of components of integrated circuits for electric signal processing and manipulation. Even more, the insights gained in this work, especially, those related to the chemical stability and effects of the MOF structure on the ion transport of composite membranes could be useful in other applications fields such as biosensing, energy conversion, drug delivery, among others.

4. Experimental Section

Materials: Zirconium tetrachloride ($ZrCl_4$), terephthalic acid (benzene-1,4-dicarboxylic acid, BDC), and hydrochloric acid (HCl) were purchased from Aldrich and used as received. Potassium chloride (KCl) and Dimethylformamide (DMF) were purchased from Anedra and used without further purification. Dowfax 2a1 was purchased from Dow Chemical. All electrochemical measurements were done in Milli-Q ultrapure water (18.2 M Ω cm^{-1}).

Nanochannel Fabrication: Nanochannels in poly(ethylene terephthalate) (PET) membranes were created by the ion-track-etching method.^[6,7,79,80] For this aim, a $12 \mu m$ PET membrane was irradiated with swift heavy ions (Au, 11.4 MeV per nucleon) and then, it was exposed to a chemical etching procedure. To create bullet-shaped nanochannels, one side of the irradiated membrane was exposed to 6 M NaOH whereas the other side was soaked in 6 M NaOH + 0.05% Dowfax 2a1. The etching temperature and time were 60 °C and 6 min, respectively. For its part, a cylindrical channel was created by exposing an irradiated membrane to 6 M NaOH at 60 °C for 4 min.

For electrochemical experiments, single-channel membranes (1 channel cm^{-2}) were employed to increase the sensitivity to the changes in the physicochemical properties of the surface. In contrast, high-pore-density membranes (10^8 channels cm^{-2}) were used for characterization by SEM microscopy and X-ray diffraction.

UiO-66 Bulk and Confined Synthesis: Bulk UiO-66 synthesis was done according to Farha et. al. at 80 °C.^[44] Powder purification was done by centrifugation in fresh DMF ($\times 3$). The solvent exchange was also done by centrifugation with ethanol ($\times 3$). Finally, the powder was dried in vacuum

at 90 °C overnight. For N_2 adsorption isotherms, the sample was activated in a vacuum oven at 150 °C for 3 h. For asymmetric interfacial growth, the protocol was slightly modified (see further details in the Supporting Information). After placing the membrane in the cell depicted in the main manuscript, the base side was exposed to a solution of 0.0551 g $ZrCl_4$ (0.236 mmol) in 6.5 mL of DMF and 0.5 mL of HCl. Tip side of the membrane was exposed to a solution of 0.0546 g (0.329 mmol) of BDC in 6.5 mL of DMF and 0.5 mL of HCl. The cell was then placed in an oven at 80 °C overnight (≈ 15 h). After cooling at room temperature, sequential washing with DMF, ethanol, and Milli-Q water was performed. After washing, the membrane was left soaking in Milli-Q water for 3 h.

Ion-Transport Experiments: Electrochemical measurements were done in a Gamry Reference 600 potentiostat with a four-electrode set-up (working, working sense, reference, and counter electrode). Measurements were conducted in a homemade conductivity cell fabricated to avoid current leakage. Both the reference and working-sense were commercial Ag/AgCl/3 M KCl electrodes, while the working and counter electrodes were Pt wires. For all the experiments, the working electrode was placed at the tip side of the membrane, while the counter electrode was placed at the base side. Moreover, the scan rate was 50 mV s^{-1} .

Material Characterization: Wide-angle X-ray scattering (WAXS) analysis of UiO-66 powder was performed in a Xeuss 1.0 HR SAXS/WAXS, XENOCOS, Grenoble setup (INIFTA, project "Nanopymes", EuropeAid/132 184/D/ SUP/AR-Contract 331-896, UNLP-CONICET) with a microfocus X-ray source and Pilatus 100K detector (Dectris, Switzerland, distance sample-detector: 97.95 mm). X-ray diffraction experiments were conducted in an X-ray diffractometer (XRD, Seifert X-ray generator, HZG-4 goniometer in Bragg-Brentano geometry). Samples were mounted with $\chi = 3^\circ$. Measurements were done at 40 kV-30 mA, with 30 s integration time.

SEM analysis was carried out in a Zeiss Gemini 500 field-emission electron microscope at different magnifications, without metalizing the samples. Membranes were explored on both sides (tip and base side). For the cross-section analysis, the samples were first exposed to UV light for ≈ 72 h and, then, broken in liquid nitrogen to prevent channel deformation. Finally, the membrane was mounted at 90° in the microscope.^[81] For the EDX measurements, a primary electron energy of 4 kV was selected. At this energy the Zr L-lines and the C and O K-lines are excited. A Bruker EDX spectrometer attached to the Zeiss Gemini 500 field-emission electron microscope was used to measure the generated X-rays and the Quantax Esprit 2.1 software was used for data analysis.

Surface-area determination was carried out with an ASAP 2020 HD88 surface area and porosity analyzer (Micromeritics).

Supporting Information

Supporting Information is available from the Wiley Online Library or from the author.

Acknowledgements

G.L. and J.A.A. contributed equally to this work. G.L. and J.A.A. acknowledge the scholarship from CONICET. M.R., W.A.M., and O.A. acknowledge the financial support from Universidad Nacional de La Plata (PPID-X867), CONICET (PIP-0370), and ANPcyT (PICT-2017-1523, PICT2018-00780 and PICT2016-1680). The irradiated PET foils are part of the experiment UMAT, which was performed at the beam line X0 at the GSI Helmholtzzentrum für Schwerionenforschung, Darmstadt (Germany) in the frame of FAIR Phase-0.

Conflict of Interest

The authors declare no conflict of interest.

Data Availability Statement

The data that support the findings of this study are available from the corresponding author upon reasonable request.

Keywords

ion current, ion-track-etching, metal–organic frameworks, nanofluidic devices, porosity

Received: August 11, 2022
Revised: September 27, 2022
Published online:

- [1] G. Pérez-Mitta, A. G. Albesa, C. Trautmann, M. E. Toimil-Molares, O. Azzaroni, *Chem. Sci.* **2017**, *8*, 890.
- [2] G. Pérez-Mitta, M. E. Toimil-Molares, C. Trautmann, W. A. Marmisollé, O. Azzaroni, *Adv. Mater.* **2019**, *31*, 1901483.
- [3] G. Laucirica, W. A. Marmisollé, M. E. Toimil-Molares, C. Trautmann, O. Azzaroni, *ACS Appl. Mater. Interfaces* **2019**, *11*, 30001.
- [4] G. Laucirica, Y. Toum Terrones, V. M. Cayón, M. L. Cortez, M. E. Toimil-Molares, C. Trautmann, W. A. Marmisollé, O. Azzaroni, *Nanoscale* **2020**, *12*, 18390.
- [5] Y. Tian, L. Wen, X. Hou, G. Hou, L. Jiang, *Chem. Phys. Chem* **2012**, *13*, 2455.
- [6] R. Spohr, *Ion Tracks and Microtechnology*, Vieweg+Teubner Verlag, Wiesbaden, Germany **1990**.
- [7] M. E. Toimil-Molares, *Beilstein J. Nanotechnol.* **2012**, *3*, 860.
- [8] G. Laucirica, M. E. Toimil-Molares, C. Trautmann, W. Marmisollé, O. Azzaroni, *Chem. Sci.* **2021**, *12*, 12874.
- [9] G. Laucirica, Y. Toum Terrones, V. Cayón, M. L. Cortez, M. E. Toimil-Molares, C. Trautmann, W. Marmisollé, O. Azzaroni, *Trends Anal. Chem.* **2021**, *144*, 116425.
- [10] S. Balme, T. Ma, E. Balanzat, J. Janot, *J. Membr. Sci.* **2017**, *544*, 18.
- [11] M. Lepoitevin, M. Bechelany, E. Balanzat, J. M. Janot, S. Balme, *Electrochim. Acta* **2016**, *211*, 611.
- [12] A. S. Peinetti, R. J. Lake, W. Cong, L. Cooper, Y. Wu, Y. Ma, G. T. Pawel, M. E. Toimil-Molares, C. Trautmann, L. Rong, B. Mariñas, O. Azzaroni, Y. Lu, *Sci. Adv.* **2021**, *7*, eabh2848.
- [13] G. Laucirica, V. M. Cayón, Y. Toum Terrones, M. L. Cortez, M. E. Toimil-Molares, C. Trautmann, W. A. Marmisollé, O. Azzaroni, *Nanoscale* **2020**, *12*, 6002.
- [14] M. Zhang, X. Hou, J. Wang, Y. Tian, X. Fan, J. Zhai, L. Jiang, *Adv. Mater.* **2012**, *24*, 2424.
- [15] S. Nasir, M. Ali, W. Ensinger, *Nanotechnology* **2012**, *23*, 225502.
- [16] I. Stassen, N. Burtch, A. Talin, P. Falcaro, M. Allendorf, R. Ameloot, *Chem. Soc. Rev.* **2017**, *46*, 3185.
- [17] M. D. Allendorf, A. Schwartzberg, V. Stavila, A. A. Talin, *Chemistry* **2011**, *17*, 11372.
- [18] G. Maurin, C. Serre, A. Cooper, G. Férey, *Chem. Soc. Rev.* **2017**, *46*, 3104.
- [19] B. F. Hoskins, R. Robson, *J. Am. Chem. Soc.* **1989**, *111*, 5962.
- [20] A. Kirchon, L. Feng, H. F. Drake, E. A. Joseph, H.-C. Zhou, *Chem. Soc. Rev.* **2018**, *47*, 8611.
- [21] A. Indra, T. Song, U. Paik, *Adv. Mater.* **2018**, *30*, 1705146.
- [22] K. A. Adegoke, N. W. Maxakato, *Mater. Today Energy* **2021**, *21*, 100816.
- [23] C. R. Quijia, R. C. Alves, G. Hanck-Silva, R. C. Galvão Frem, G. Arroyos, M. Chorilli, *Crit. Rev. Microbiol.* **2022**, *48*, 161.
- [24] P. Pashazadeh-Panahi, S. Belali, H. Sohrabi, F. Oroojalian, M. Hashemzaei, A. Mokhtarzadeh, M. de la Guardia, *Trends Anal. Chem.* **2021**, *141*, 116285.
- [25] C. Peng, Y. Xue, X. Zhu, Y. Fan, J. Li, E. Wang, *Anal. Chem.* **2022**, *94*, 1465.
- [26] J. Zhu, L. Qin, A. Uliana, J. Hou, J. Wang, Y. Zhang, X. Li, S. Yuan, J. Li, M. Tian, J. Lin, B. van der Bruggen, *ACS Appl. Mater. Interfaces* **2017**, *9*, 1975.
- [27] W. Yang, Y. Zhu, Z. Sun, C. Gao, L. Xue, *Adv. Mater. Interfaces* **2019**, *6*, 1901482.
- [28] H. Zhang, J. Hou, Y. Hu, P. Wang, R. Ou, L. Jiang, J. Z. Liu, B. D. Freeman, A. J. Hill, H. Wang, *Sci. Adv.* **2018**, *4*, eaaq0066.
- [29] J. Lu, H. Zhang, J. Hou, X. Li, X. Hu, Y. Hu, C. D. Easton, Q. Li, C. Sun, A. W. Thornton, M. R. Hill, X. Zhang, G. Jiang, J. Z. Liu, A. J. Hill, B. D. Freeman, L. Jiang, H. Wang, *Nat. Mater.* **2020**, *19*, 767.
- [30] J. Lu, H. Zhang, X. Hu, B. Qian, J. Hou, L. Han, Y. Zhu, C. Sun, L. Jiang, H. Wang, *ACS Nano* **2021**, *15*, 1240.
- [31] X. Li, H. Zhang, P. Wang, J. Hou, J. Lu, C. D. Easton, X. Zhang, M. R. Hill, A. W. Thornton, J. Z. Liu, B. D. Freeman, A. J. Hill, L. Jiang, H. Wang, *Nat. Commun.* **2019**, *10*, 2490.
- [32] L. Xin, D. Zhang, K. Qu, Y. Lu, Y. Wang, K. Huang, Z. Wang, W. Jin, Z. Xu, *Adv. Funct. Mater.* **2021**, *31*, 2104629.
- [33] X. Li, H. Zhang, H. Yu, J. Xia, Y. Zhu, H. Wu, J. Hou, J. Lu, R. Ou, C. D. Easton, C. Selomulya, M. R. Hill, L. Jiang, H. Wang, *Adv. Mater.* **2020**, *32*, 2001777.
- [34] Z.-Y. Jiang, H.-L. Liu, S. A. Ahmed, S. Hanif, S.-B. Ren, J.-J. Xu, H.-Y. Chen, X.-H. Xia, K. Wang, *Angew. Chem.* **2017**, *129*, 4845.
- [35] J. Lu, H. Xu, H. Yu, X. Hu, J. Xia, Y. Zhu, F. Wang, H.-A. Wu, L. Jiang, H. Wang, *Sci. Adv.* **2022**, *8*, eabl5070.
- [36] M. Usman, M. Ali, B. A. Al-Maythaly, A. S. Ghanem, O. W. Saadi, M. Ali, M. A. Jafar Mazumder, S. Abdel-Azeim, M. A. Habib, Z. H. Yamani, W. Ensinger, *ACS Appl. Mater. Interfaces* **2020**, *12*, 49992.
- [37] Y.-C. Liu, L.-H. Yeh, M.-J. Zheng, K. C.-W. Wu, *Sci. Adv.* **2021**, *7*, eabe9924.
- [38] K. Xie, Q. Fu, P. A. Webley, G. G. Qiao, *Angew. Chem., Int. Ed.* **2018**, *57*, 8597.
- [39] J. A. Allegretto, A. Iborra, J. M. Giussi, C. Bilderling, M. Ceolín, S. Moya, O. Azzaroni, M. Rafti, *Chemistry* **2020**, *26*, 12388.
- [40] J. A. Allegretto, M. Arcidiácono, P. Y. Steinberg, P. C. Angelomé, O. Azzaroni, M. Rafti, *J. Phys. Chem. C* **2022**, *126*, 6724.
- [41] H. Fei, S. Pullen, A. Wagner, S. Ott, S. M. Cohen, *Chem. Commun.* **2015**, *51*, 66.
- [42] C. Zhang, Y. Zhao, Y. Li, X. Zhang, L. Chi, G. Lu, *Chem Asian J* **2016**, *11*, 207.
- [43] Y. Huang, C. Tao, R. Chen, L. Sheng, J. Wang, *Nanomaterials* **2018**, *8*, 676.
- [44] M. J. Katz, Z. J. Brown, Y. J. Colón, P. W. Siu, K. A. Scheidt, R. Q. Snurr, J. T. Hupp, O. K. Farha, *Chem. Commun.* **2013**, *49*, 9449.
- [45] J. H. Cavka, S. Jakobsen, U. Olsbye, N. Guillou, C. Lamberti, S. Bordiga, K. P. Lillerud, *J. Am. Chem. Soc.* **2008**, *130*, 13850.
- [46] L. Valenzano, B. Civalieri, S. Chavan, S. Bordiga, M. H. Nilsen, S. Jakobsen, K. P. Lillerud, C. Lamberti, *Chem. Mater.* **2011**, *23*, 1700.
- [47] M. Kim, S. M. Cohen, *CrystEngComm* **2012**, *14*, 4096.
- [48] M. J. Cliffe, W. Wan, X. Zou, P. A. Chater, A. K. Kleppe, M. G. Tucker, H. Wilhelm, N. P. Funnell, F.-X. Coudert, A. L. Goodwin, *Nat. Commun.* **2014**, *5*, 4176.
- [49] L. Liu, Z. Chen, J. Wang, D. Zhang, Y. Zhu, S. Ling, K.-W. Huang, Y. Belmabkhout, K. Adil, Y. Zhang, B. Slater, M. Eddaoudi, Y. Han, *Nat. Chem.* **2019**, *11*, 622.
- [50] G. C. Shearer, S. Chavan, S. Bordiga, S. Svelle, U. Olsbye, K. P. Lillerud, *Chem. Mater.* **2016**, *28*, 3749.
- [51] Z. S. Siwy, *Adv. Funct. Mater.* **2006**, *16*, 735.
- [52] E. B. Kalman, I. Vlassiuk, Z. S. Siwy, *Adv. Mater.* **2008**, *20*, 293.
- [53] H. Daiguji, Y. Oka, K. Shirono, *Nano Lett.* **2005**, *5*, 2274.
- [54] M. Ali, P. Ramirez, H. Q. Nguyen, S. Nasir, J. Cervera, S. Mafe, W. Ensinger, *ACS Nano* **2012**, *6*, 3631.
- [55] G.-C. Liu, L.-B. Song, X.-H. Wang, C.-Q. Li, B. Liu, Y.-D. Zhao, W. Chen, *Anal. Chim. Acta* **2020**, *1117*, 35.
- [56] A. Höltzel, U. Tallarek, *J. Sep. Sci.* **2007**, *30*, 1398.
- [57] I. Rubinstein, B. Zaltzman, *Phys. Rev. E* **2000**, *62*, 2238.

- [58] S. J. Kim, Y.-C. Wang, J. H. Lee, H. Jang, J. Han, *Phys. Rev. Lett.* **2007**, *99*, 044501.
- [59] R. B. Schoch, J. Han, P. Renaud, *Rev. Mod. Phys.* **2008**, *80*, 839.
- [60] S. J. Kim, Y.-A. Song, J. Han, *Chem. Soc. Rev.* **2010**, *39*, 912.
- [61] F. C. Leinweber, M. Pfafferodt, A. Seidel-Morgenstern, U. Tallarek, *Anal. Chem.* **2005**, *77*, 5839.
- [62] J. Gao, W. Guo, D. Feng, H. Wang, D. Zhao, L. Jiang, *J. Am. Chem. Soc.* **2014**, *136*, 12265.
- [63] Y. He, D. Gillespie, D. Boda, I. Vlassiuk, R. Eisenberg, Z. Siwy, *J. Am. Chem. Soc.* **2009**, *131*, 5194.
- [64] W. Morris, S. Wang, D. Cho, E. Auyeung, P. Li, O. K. Farha, C. A. Mirkin, *ACS Appl. Mater. Interfaces* **2017**, *9*, 33413.
- [65] B. Shan, J. B. James, M. R. Armstrong, E. C. Close, P. A. Letham, K. Nikkhah, Y. S. Lin, B. Mu, *J. Phys. Chem. C* **2018**, *122*, 2200.
- [66] M. J. van Vleet, T. Weng, X. Li, J. R. Schmidt, *Chem. Rev.* **2018**, *118*, 3681.
- [67] H. Xu, S. Sommer, N. L. N. Broge, J. Gao, B. B. Iversen, *Chemistry* **2019**, *25*, 2051.
- [68] H. Zhang, X. Hou, Z. Yang, D. Yan, L. Li, Y. Tian, H. Wang, L. Jiang, *Small* **2015**, *11*, 786.
- [69] G. Pérez-Mitta, A. Albesa, F. M. Gilles, M. E. Toimil-Molares, C. Trautmann, O. Azzaroni, *J. Phys. Chem. C* **2017**, *121*, 9070.
- [70] M. Ali, P. Ramirez, S. Mafe, R. Neumann, W. Ensinger, *ACS Nano* **2009**, *3*, 603.
- [71] A. J. Bard, L. R. Faulkner, H. S. White, *Electrochemical Methods*, John Wiley & Sons, Hoboken, NJ, USA **2001**.
- [72] R. C. Klet, Y. Liu, T. C. Wang, J. T. Hupp, O. K. Farha, *J. Mater. Chem. A* **2016**, *4*, 1479.
- [73] R. B. Schoch, P. Renaud, *Appl. Phys. Lett.* **2005**, *86*, 253111.
- [74] J. Li, D. Li, *ACS Appl. Mater. Interfaces* **2021**, *13*, 48208.
- [75] J. A. Allegretto, J. Dostalek, M. Rafti, B. Menges, O. Azzaroni, W. Knoll, *J. Phys. Chem. A* **2019**, *123*, 1100.
- [76] L. Feng, K.-Y. Wang, G. S. Day, M. R. Ryder, H.-C. Zhou, *Chem. Rev.* **2020**, *120*, 13087.
- [77] M. Ding, X. Cai, H.-L. Jiang, *Chem. Sci.* **2019**, *10*, 10209.
- [78] K. Leus, T. Bogaerts, J. de Decker, H. Depauw, K. Hendrickx, H. Vrielinck, V. van Speybroeck, P. van der Voort, *Microporous Mesoporous Mater.* **2016**, *226*, 110.
- [79] G. Laucirica, G. Pérez-Mitta, M. E. Toimil-Molares, C. Trautmann, W. A. Marmisollé, O. Azzaroni, *J. Phys. Chem. C* **2019**, *123*, 28997.
- [80] V. M. Cayón, G. Laucirica, Y. Toum Terrones, M. L. Cortez, G. Pérez-Mitta, J. Shen, C. Hess, M. E. Toimil-Molares, C. Trautmann, W. A. Marmisollé, O. Azzaroni, *Nanoscale* **2021**, *13*, 11232.
- [81] P. Y. Apel, I. v. Blonskaya, S. N. Dmitriev, O. L. Orelovitch, A. Presz, B. A. Sartowska, *Nanotechnology* **2007**, *18*, 305302.